Higher key rate in asymmetric quantum-classical integrated measurement-device-independent quantum-key-distribution systems

Wei-Xin Xie,[1,2,†] Guan-Jie Fan-Yuan,[1,2,†] Ze-Hao Wang,[1,2] Feng-Yu Lu,[1,2] Jia-Xuan Li,[1,2] Shuang Wang,[1,2,3,*] Zhen-Qiang Yin,[1,2,3] Wei Chen,[1,2,3] De-Yong He,[1,2,3] Guang-Can Guo,[1,2,3] and Zheng-Fu Han[1,2,3]

[1] *CAS Key Laboratory of Quantum Information, University of Science and Technology of China, Hefei, 230026 Anhui, China*

[2] *CAS Center for Excellence in Quantum Information and Quantum Physics, University of Science and Technology of China, Hefei, 230026 Anhui, China*

[3] *Hefei National Laboratory, University of Science and Technology of China, Hefei, 230088 Anhui, China*

(Received 28 April 2023; revised 16 August 2023; accepted 2 November 2023; published 20 November 2023)

Integrating measurement-device-independent quantum key distribution (MDI QKD) with classical networks guarantees security and economy. Unfortunately, the performance of MDI QKD, suppressed though it is by network asymmetry, is further degraded by the addition of integration noise. As a consequence, symmetric systems are always believed to be better for a higher key rate. However, we reveal a counterintuitive fact that asymmetric MDI QKD has better performance in integrated systems. Modeling the mechanism of the asymmetric effect in integrated MDI systems and analyzing the noise-suppression effect of asymmetric structures, we observe an unanticipated increase of the key rate up to 260%, giving a conclusion diametrically opposite that for the original system. The phenomenon found and the proposed analytical model provide a method for noise suppression and performance improvement, permitting high adaptability for realistic asymmetric networks.

DOI: 10.1103/PhysRevApplied.20.054042

I. INTRODUCTION

Quantum-key-distribution (QKD) networks aim at realizing multiuser secure key sharing [1–14]. Traditional communication integrated with QKD systems will effectively increase the security level, and the economic cost of deploying reliable QKD networks based on integrated systems will be cheaper. The core concept of integration is transmitting quantum and classical signals in the same optical fiber, which was first realized by Townsend and coworkers [15]. After dealing with the impact of cross-channel noise from classical channels, we construct the QKD networks economically. Previous work was based mainly on the BB84 protocol and its variants [15–21]. However, the measurement-side security of the BB84 protocol is an annoying shortcoming, although the systems are mature enough for a high key rate. In 2012, with the aim of fighting against an attack on the measurement side [22–26], a measurement-device-independent (MDI) QKD protocol was proposed [27,28]. The special structure of MDI QKD determines that this protocol is suitable for building star-type QKD networks. Therefore, promoting the integrated deployment of the MDI protocol is imperative. In 2019, an integration scheme for an MDI QKD protocol was proposed [29], and this establishes the basic framework of an integrated MDI system. The research that followed focused mainly on field tests [30] and long-distance systems [31]. Differently from the BB84 protocol, the MDI protocol, inserting extra nodes, introduces new problems for the integration scheme; for instance, asymmetric structure and more-complicated analysis for noise.

To construct a practical integrated MDI system, one must face two obstacles, noise and asymmetry. For noise, the power for classical signals is about 7–9 orders of magnitude higher than the power for quantum signals. Quantum subsystems are sensitive to the influences of noise from classical channels. Because of the nonlinear effect of optical fiber, signal photons will generate additional photons in other channels, which become the main component of cross-channel noise. Spontaneous-Raman-scattering (SPRS) noise [32], the spectral width of which is wide enough to cover the whole communication band of a QKD system, is the dominant noise. Cross-channel noise will increase the background noise level, causing higher key-rate consumption during the error-correction process. For asymmetry, to adapt a complex communication environment, the integrated MDI system needs to be designed with an asymmetric structure

*wshuang@ustc.edu.cn

†These authors contributed equally.

[33–36]. There is no reason for two senders (Alice and Bob) to have the same distance from Charlie, on the measurement side. In other words, the transmission efficiency may not always be the same. According to previous research on the original MDI system, the deviation between transmission efficiency can increase the quantum bit error rate in signal states [33]. Use of an asymmetric protocol [33] can mitigate the impact; however, symmetric systems are regarded to be better under a severer integrated environment. Most studies are based on symmetric-fiber or symmetric-attenuation systems to perform integration for the MDI protocol [29,30].

It seems that all the characteristics are negative for the performance of a QKD system. This conclusion is deceptive because we treat these characteristics in their own environment. However, the integrated MDI system is more than a trivial addition of two systems. The cross-channel noise can be regulated by the channel length, which is the object of asymmetric allocation. That means it is possible to suppress the noise level by adjusting the asymmetry of the integrated MDI system. The asymmetric effect brings about noise suppression for the integrated system and a key-rate decrease for the original MDI system. Balancing this trade-off is positive for proposing integrated MDI schemes with better performance and practicability. We describe this concept as two negatives make an affirmative.

In this work, we observe a higher key rate in an asymmetric integrated MDI system than in a symmetric one. This paper is organized as follows. The model of an asymmetric integrated MDI QKD system is introduced in Sec. II. We are surprised to observe that the asymmetry has the potential to suppress the SPRS noise; therefore, we expected that there would be a key-rate increase in the asymmetric structure. A relative demonstration and further discussions are given in Sec. III. Two opposite factors caused by asymmetry are discovered that quantitatively explain the key-rate increase in asymmetric systems. Further calculations considering finite-size effects are given in Sec. IV, and they demonstrate that our conclusions are still valid in practical scenarios. The conclusions and expectations are presented in Sec. V. Suitable use of the asymmetric effect will effectively optimize the integrated MDI schemes. Our study reveals an opposite key-rate evolution in integrated MDI systems compared with the original system, making practical and high-performance systems possible, which is beneficial for the construction of practical QKD networks.

II. THEORETICAL MODEL OF AN ASYMMETRIC INTEGRATED MDI QKD SYSTEM

In Sec. II A, we determine the structure of the asymmetric integrated MDI system and integration scheme. Necessary modeling information is given in Sec. II B.

A. Structural framework of the asymmetric integrated MDI QKD system

The structural framework of the asymmetric integrated MDI system is shown in Fig. 1. The users, Alice and Bob, execute the MDI QKD protocol by sending quantum signals (blue arrows) to Charlie, and they also transmit classical signals (red and orange curves) to each other. Quantum and classical signals are transmitted in the same single-mode fiber (SMF). Aiming at making full use of untrust advantage in MDI systems, we relaxed the restrictions on the location assignment of untrusted Charlie in the system. The measurement nodes have lower security requirements, which gives them greater maneuverability. Moreover, in future quantum-classical integrated MDI networks, operators will need to choose the optimal measurement-node layout schemes for a fixed customer distribution in advance. For the considerations above, we fixed Alice and Bob, permitting Charlie to be flexible, so as to realize the asymmetric allocation. The classical communication function of Charlie is canceled for simplicity. Only Alice and Bob execute classical communication. (Strictly speaking, Charlie still needs communication for service function, but those signals are too weak to have a considerable influence compared with the original classical signals.)

We discuss two integrated cases. The first one is unidirectional, which permits only Alice to send classical signals, with launch power P_A. This case corresponds to the red arrows in Fig. 1. The other case permits bidirectional transmission for classical signals, which means Bob also sends classical signals, with launch power P_B, as the orange arrow in Fig. 1. Classical signals pass Charlie without any modulation.

B. Asymmetric model of the integrated MDI system

Here we give the key-rate formula for the original MDI QKD scheme [31,37,38]:

$$\mathcal{R}_{\text{original}} = \frac{1}{2}\{Q_{11}[1 - H(e_{11})] - f_e Q_{\text{rect}} H(E_{\text{rect}})\}, \quad (1)$$

where Q_{11} and e_{11} denote the gain and quantum bit error rate of a single-photon event; Q_{rect} and E_{rect} denote the gain and quantum bit error rate in a rectilinear basis; $H(x)$ is a binary Shannon function, whose form is $H(x) = -x\log_2(x) - (1-x)\log_2(1-x)$; and f_e is the error-correction efficiency. The specific forms of the gain and error rate are given in Appendix A.

Referring to previous work [33–36], we rewrite the transmission efficiency η_A and η_B by introducing the channel asymmetric index $\theta = L_{AC}/L_{BC}$ as

$$\eta_A = \eta_m 10^{\frac{-\alpha L\theta}{10(1+\theta)}}, \quad \eta_B = \eta_m 10^{\frac{-\alpha L}{10(1+\theta)}}, \quad (2)$$

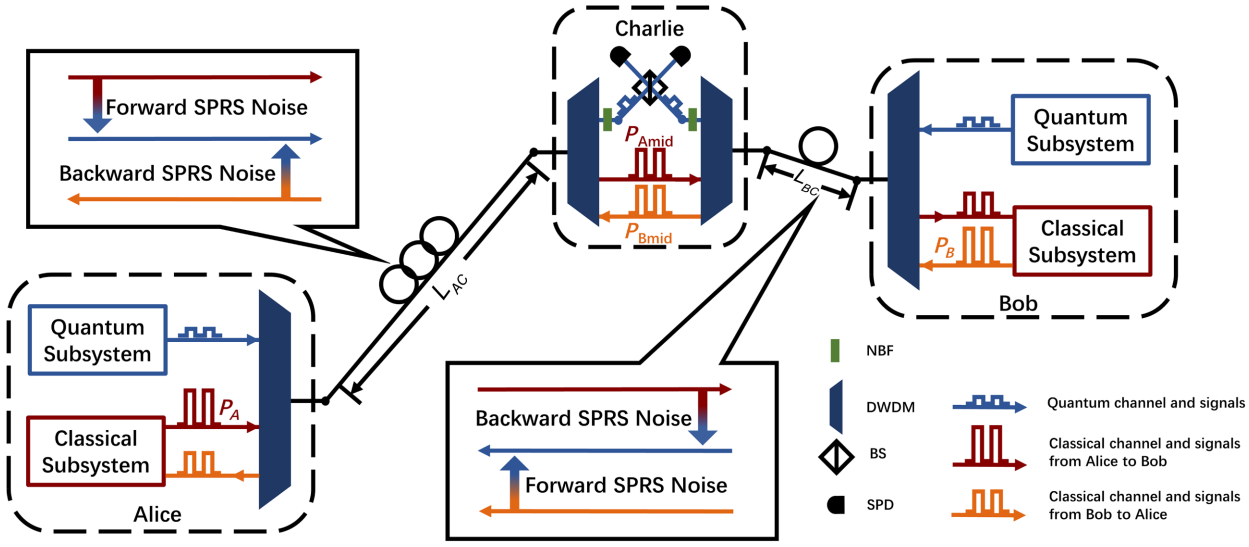

FIG. 1. Framework of the asymmetric integrated MDI QKD system. The whole system of Alice and Bob can be divided into quantum subsystems and classical subsystems. The quantum subsystems send modulated quantum signals to Charlie, and the classical subsystems transmit classical signals with launch power P_A or P_B and receive incoming signals. Quantum channels and classical channels are coupled into the same SMF through DWDM. Signals received by Charlie are divided by demultiplexers, and the quantum channels are filtered by a narrowband filter (NBF) placed in front of the Bell-state-measurement device. To facilitate the calculation, we denote the classical power at Charlie as P_{Amid} and P_{Bmid}. The dialog boxes display the SPRS-noise formation process in two different fibers. BS, beam splitter.

where η_m is the efficiency of the measurement side, including the insertion loss and the detection efficiency of the single-photon detector (SPD), α is the attenuation coefficient of the SMF, and $L = L_{AC} + L_{BC}$, where L_{AC} (L_{BC}) is the fiber length between Alice (Bob) and Charlie. The transmission efficiencies contained in the gain and the error rate are directly influenced by asymmetric allocation.

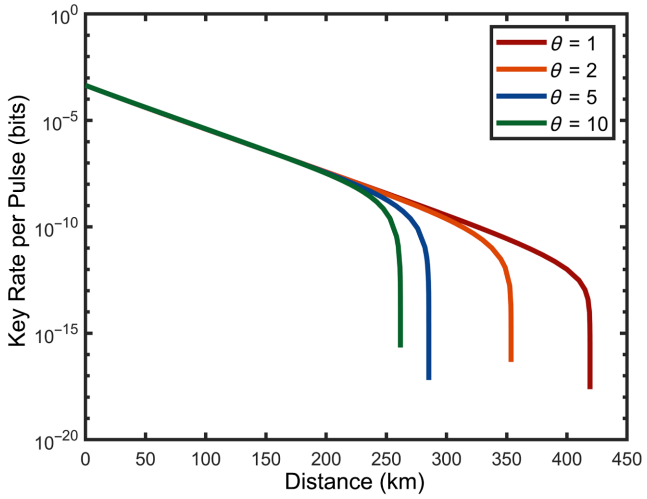

FIG. 2. Key rate of the asymmetric original MDI QKD system with different asymmetric structures. Secure-key-rate curves with different θ (different degrees of asymmetry) are given in different colors.

Replacing the transmission efficiencies with new forms in Eq. (2), we can analyze our model with asymmetric channels.

Simulations of key rate in the original MDI system are shown in Fig. 2. The performance of the original MDI system is obviously suppressed by asymmetric channels. The parameters we used in this paper are listed in Table I.

The background count rate, Y_0, comes mainly from the response to the dark count of the detectors and background noise. It plays a critical role in integrated processing. $Y_0 = 2p_d$ [31,37] in the original MDI system, where p_d is the dark count rate of the SPD. The noise description of Y_0 is the key to our integrated model. In integrated MDI systems, Y_0 is written as [29–31]

$$Y_0 = 2p_d + p_x. \tag{3}$$

TABLE I. Parameters used in this paper.

Parameter	Value
η_m	20%
f_e	1.15
e_d	2%
p_d	5×10^{-8} per window
ρ	1.59×10^{-9} km^{-1} nm^{-1}
T_d	0.5 ns
λ_q	1550 nm
$\Delta\lambda$	0.2 nm
α	0.2 dB/km

The SPRS noise is treated as shot noise with a Poisson distribution. Considering weak intensity approximation, the noise photon count rate p_x is equal to the detected average photon number N_x. The subscript x represents unidirectional and bidirectional cases.

In the unidirectional case, quantum signals and classical signals propagate in the fiber between Alice (Bob) and Charlie in the same (a different) direction, which results in forward (backward) noise (the definitions are given in Appendix B). Therefore, we should treat these types of noise with different parameters. For example, the launch power of forward noise is P_A, while the launch power of backward noise is P_{Amid}, which is the attenuation of P_A due to the channel loss. The fiber length for forward (backward) noise is L_{AC} (L_{BC}). The same discussion can be used in the bidirectional case. The bidirectional integrated scheme will cause another asymmetry, power asymmetry. For convenience, we introduce the power asymmetric index $\gamma = P_A/P_B$ to describe it.

We can now calculate the noise photon number per window N_x with the formulas

$$\begin{aligned} N_{\text{uni}} &= N_{\text{forward}}(L_{AC}, P_A) + N_{\text{backward}}(L_{BC}, P_{\text{Amid}}), \\ N_{\text{bi}} &= N_{\text{forward}}(L_{AC}, P_A) + N_{\text{backward}}(L_{BC}, P_{\text{Amid}}) \\ &\quad + N_{\text{forward}}(L_{BC}, P_B) + N_{\text{backward}}(L_{AC}, P_{\text{Bmid}}). \end{aligned} \tag{4}$$

Details of the methods for calculating N_{forward} and N_{backward} are given in Appendix B.

Specifically, we propose three noise models: a unidirectional model, a bidirectional model with symmetric power, and a bidirectional model with asymmetric power. Figures 3(a)–3(c) show the noise level in the different noise models. We find that the noise photon number increases in the early stage and then decreases with the extension of fiber length.

Without loss of generality, we discuss Fig. 3(a) in detail. The noise level reaches a maximum at about 20–40 km, and the asymmetry causes a left shift of the peaks. The value of 40 km comes from the basic noise model introduced in Appendix B. For forward and backward noise, the highest level is reached at 20 km. The asymmetry makes the forward noise dominant, which changes the typical value to 20 km. The more intense the asymmetric effect is, the lower is the noise we get in the unidirectional case. However, in the bidirectional case, we find that at long distances, the asymmetric structure cannot suppress the noise. A more-extreme asymmetric structure (both in fiber length and in power) has greater potential to suppress the noise. The three models can be connected by the index γ: $\gamma = +\infty$ corresponds to the unidirectional case, $\gamma = 1$ corresponds to the bidirectional case with symmetric power, and other values of γ correspond to the bidirectional case with asymmetric power. The relationship is displayed in Fig. 3(d), and we also observe the noise-suppression potential of power asymmetry.

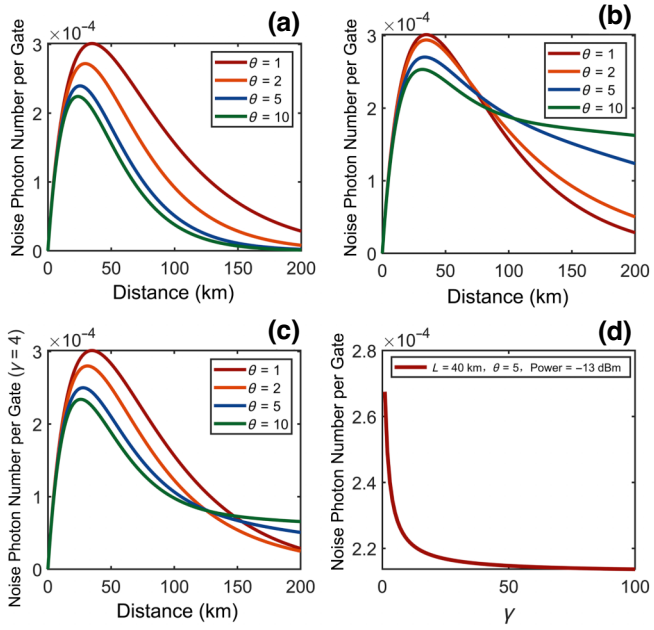

FIG. 3. Noise models considering the asymmetric effect. The total launch power is −13 dBm. (a) Unidirectional noise model. (b) Bidirectional model with symmetric power. (c) Bidirectional model with asymmetric power, $\gamma = 4$. (d) Relationship between the three models: $L = 40$ km and $\theta = 5$.

After rewriting Y_0 and η_A (η_B), we establish the model of an asymmetric integrated MDI system. According to the results, the noise can be suppressed by the asymmetric structure, which is a positive factor for the integrated system. Naturally, we expect that the asymmetric integrated MDI system could obtain a higher key rate, but the accuracy still needs to be verified (see Sec. III) for the key-rate suppression in Fig. 2.

III. ASYMMETRIC EFFECT IN THE INTEGRATED MDI SYSTEM

For convenience, we discuss the unidirectional integrated system as an example. We start by answering the question proposed at the end of Sec. II. A simple verification of key-rate increase is done in Sec. III A. The question of why the asymmetry increases the key rate is answered in Sec. III B.

A. Feasibility analysis of higher performance with an asymmetric structure

If we fix the system parameters given in Table I, the key rate will be a function of θ, L, and P_A. A criterion is required for judging whether an increase is possible. The derivative value of the key-rate function when $\theta = 1$, $\partial\mathcal{R}/\partial\theta\big|_{\theta=1}$, is suitable. It reveals the potential of our

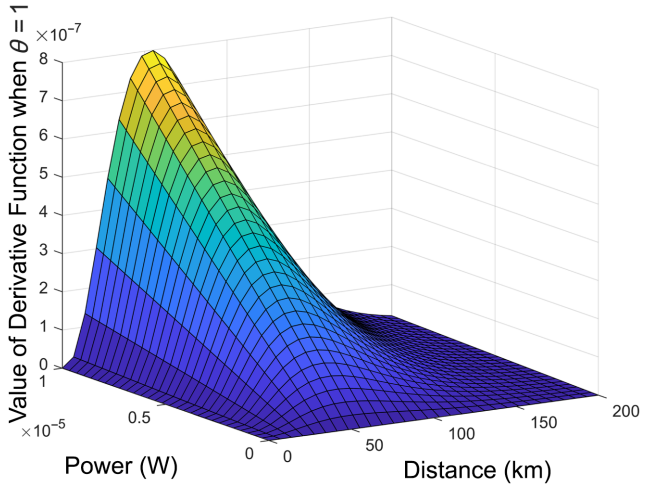

FIG. 4. Value of the derivative function when $\theta = 1$. The transmission length is scanned from 0 to 200 km, and the maximum power is 5×10^{-5} W (−13 dBm). The maximum length, 200 km, is determined from the results in Fig. 2. The maximum power, −13 dBm, is close to the maximum power the MDI system can tolerate at 200 km with the parameters in Table I. Thus, all the points we scan can produce a positive key rate.

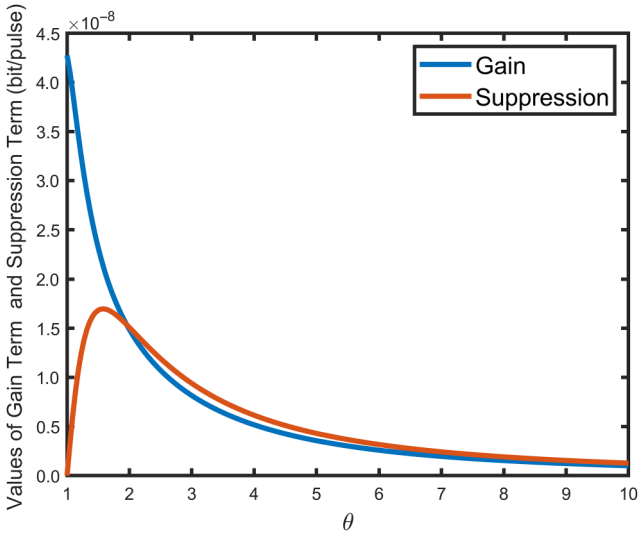

FIG. 5. Different terms of the derivative function. The blue curve represents the gain term and the red curve represents the suppression term in the derivative function. The transmission length and power are set as 200 km and 5×10^{-5} W (−13 dBm), respectively. Here we use the blue and red curves to represent $\frac{\partial Y_0}{\partial \theta} C_1(\theta, L, P_A)$ and $-\frac{\partial \eta_A}{\partial \theta} C_2(\theta, L, P_A)$, respectively, for intuitive comparison.

scheme in different integrated environments. A positive value means the asymmetry can be used to get higher performance. A nonpositive value brings about trivial results.

We show the derivative value with different integration environments in Fig. 4. Fortunately, if we ignore the precision of the algorithm, all the values are non-negative and the points show positive values occupy a wide range in the scanning area. The results in Fig. 4 indicate that the expectations in Sec. II are verified. Another conclusion from Fig. 4 deserves mention. The definition of the derivative tells us that $\partial\mathcal{R}/\partial\theta\big|_{\theta=1}$ contains the evolution law along the direction where $\theta > 1$. For the reverse direction, $-\partial\mathcal{R}/\partial\theta\big|_{\theta=1}$ tells us the behavior of the key rate when $\theta < 1$. Negative values indicate the key rate will decrease when $\theta < 1$. Obviously this structure makes the backward noise, which maintains a high level of saturation over a long-enough distance, dominant. Therefore, we find a higher SPRS-noise level. To explore the key-rate increase in asymmetric systems, we discuss only the situation where $\theta > 1$.

B. Two competitive factors in the asymmetric integrated system

We now propose two vague concepts whereby the asymmetry brings about positive and negative factors for the integrated system. A quantitative description is required so that we can have better understanding of the improvement. The questions would be difficult if we focus only on the formula for the key rate, for the two factors are strongly coupled. However, if we instead search in the space of the derivative function, the question above will be solved easily.

The quantity $\eta_A\eta_B$ has nothing to do with the channel asymmetric index θ, so we can derive the relationship

$$\frac{\partial \eta_A\eta_B}{\partial\theta} = \eta_A \frac{\partial \eta_B}{\partial\theta} + \eta_B \frac{\partial \eta_A}{\partial\theta} = 0. \tag{5}$$

Then the derivative function for θ can be written as

$$\frac{\partial\mathcal{R}}{\partial\theta} = \frac{\partial Y_0}{\partial\theta} C_1(\theta, L, P_A) + \frac{\partial\eta_A}{\partial\theta} C_2(\theta, L, P_A). \tag{6}$$

The factors are decoupled in Eq. (6). More details can be found in Appendix A.

Equation (6) can be regarded as a gain-suppression function, for it reveals the relationship between gain and suppression for the asymmetric effect. We call the first term, which contains $\partial Y_0/\partial\theta$, the "gain term," for it shows the suppression of noise. The second term contains $\partial\eta_A/\partial\theta$ and is called the "suppression term," for it shows the unbalance of transmission efficiencies. The two factors are combined by two coefficients C_1 and C_2, which will be confirmed by the system parameters. The detailed behaviors of the gain term and the suppression term are shown in Fig. 5.

With a higher asymmetry level, the gain term always decreases, and the suppression term increases in the early stage and then decreases. The intersection of the two curves represents the optimal asymmetric structure of the

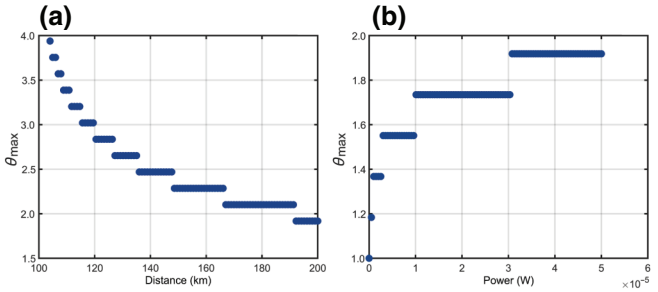

FIG. 6. Behavior of θ_{max} in different conditions. (a) Behavior of θ_{max} for different transmission distances; the power is 5×10^{-5} W (−13 dBm). (b) Behavior of θ_{max} for different powers; the transmission distance is 200 km.

integrated system. We use θ_{max} to note the intersection. For convenience, we divide the θ space into two zones by θ_{max}. The zone before the intersection is called the "gain zone," for the gain term is the dominant quantity, and the key rate maintains an upward trend. The zone after the intersection is called the "suppression zone." The suppression term is slightly stronger than the gain term even though they evolve with the same level in the suppression zone, so the key rate starts to decrease. The range of the two zones will vary with different integrated environments.

In practical applications, it is worth analyzing the behavior of θ_{max}. We simulate θ_{max} with different integration environments in Fig. 6. The behavior of θ_{max} shows differences. Figure 6(a) shows a decrease of θ_{max} with longer distances, while Fig. 6(b) shows an increase of θ_{max} with higher power. According to Fig. 2, the suppression will be stronger at long distances. A conservative asymmetric structure has more potential to balance two factors, and the best performance will be located at low θ_{max} with long distances. Because of the proportional relationship between power and noise level, higher power brings about intense suppression of noise, and thus a radical asymmetric structure is helpful, and that is why we see an increase in the power domain.

In this section, besides the verification of improvement feasibility, we introduced the gain term and the suppression term to explain why and how asymmetry increases the performance. The discussion was for the asymptotic case, and more consideration for practicability is provided in Sec. IV.

IV. PRACTICAL EXPANSION OF THE ASYMMETRIC INTEGRATED SCHEME

In practical MDI QKD systems, it is necessary to consider the finite-key effect and decoy-state method [39–42]. Here we use the four-intensity decoy MDI QKD method to analyze the performance of our scheme in a practical communication environment. The key-rate formulas are given

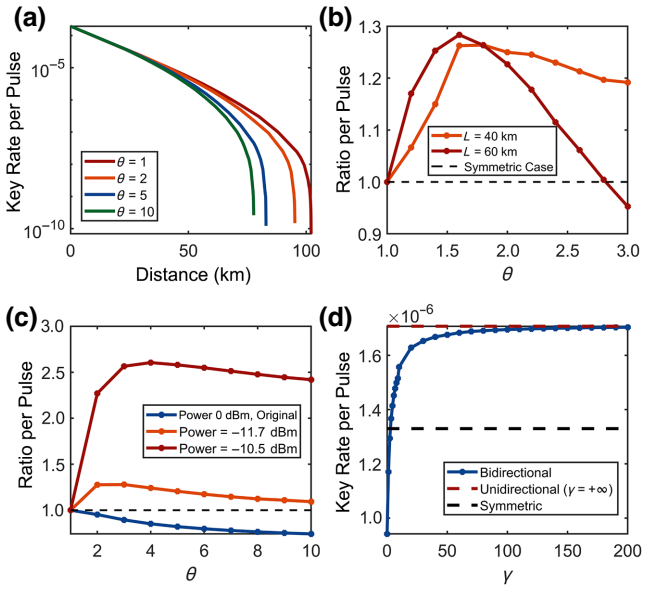

FIG. 7. Asymmetric key rate in a practical environment. (a) Key rate of the original asymmetric MDI system. (b) Key-rate ratio of the integrated MDI system with different transmission lengths; the classical power is −13 dBm. (c) Key-rate ratio of the integrated MDI system with different classical powers; the transmission length is 40 km. (d) Key rate of the integrated MDI system with different power asymmetry; the transmission length is 40 km, the classical power is −11.7 dBm, and $\theta = 3$.

as [42]

$$
\begin{aligned}
R^*(H,M) = p_{ZA}p_{ZB}\Big\{ & a_1^Z b_1^Z s_{11,Z}^L \left[1 - H\left(e_{11}^{\mathrm{ph},U}\right)\right] \\
& - f_e S_{zz} H(E_{zz})\Big\} \\
& - \frac{1}{N}\left(\log_2\frac{8}{\epsilon_{\mathrm{cor}}} + 2\log_2\frac{2}{\epsilon'\hat{\epsilon}} + 2\log_2\frac{1}{2\epsilon_{PA}}\right), \\
R = \min & R^*(H,M), \\
H \in & [H^L, H^U], \\
M \in & [M^L, M^U]. \qquad (7)
\end{aligned}
$$

All quantities given in Eq. (7) are explained in Ref. [42]. With the same parameters as in Table I, we simulate the key rate of the original MDI system in Fig. 7(a). The total pulse number N is set as 10^{11} and the total secure efficiency $\epsilon_{\mathrm{total}}$ is 10^{-10}. The key rate decreases greatly compared with the case in Fig. 2 because of the finite-key effect.

We also simulate the key rate with different integration environments in the unidirectional case in Figs. 7(b) and 7(c). For intuitive presentation, we replace the key rate with the key-rate ratio, $\mathcal{R}(\theta = x)/\mathcal{R}(\theta = 1)$. As expected, we observe a prominent key-rate increase in asymmetric systems, and θ_{max} has the same behavior as in Sec. III. Typically, the highest increase we achieved is about 260% with −10.5-dBm launch power at 40 km. The parameters

are determined by Fig. 7(a) so as to guarantee positive key production in all simulation conditions.

According to the discussion above, we note that the key-rate increase is environment related. The increase can be evaluated by the maximum increase and the coverage interval. Figure 7(b), with different distances, shows typical examples. Systems with 60 km can result in greater maximum increase but the coverage interval is relatively limited. The results change in systems with 40 km. Higher sensitivity to noise and stronger suppression from asymmetry of long-distance systems can explain this phenomenon. More details and further discussion are provided in Appendix C. Exploration of the bidirectional case is shown in Fig. 7(d). This case introduces power asymmetry. As expected in Sec. II, the key rate evolves with a trend opposite that of noise. The asymmetric power scheme can also increase the key rate effectively. These results confirm the discussion about the relationship among different noise models we mentioned in Sec. II.

All the results in Fig. 7 demonstrate the feasibility of our scheme in a practical integrated MDI system.

V. CONCLUSION

In summary, we observe a higher key rate in asymmetric systems through investigation of the asymmetry in integrated MDI systems. Starting with the noise suppression of asymmetry, we predict a higher key rate in asymmetric systems. Moreover, we verify our expectation and answer the question of how the asymmetry affects the systems. A finite-size effect is considered to prove the practicability of our conclusion. At the same time, our analysis is also applicable to other protocols with untrusted nodes; for example, twin-field QKD [43,44]. The integrated works of those protocols will not concern the asymmetric effect anymore if we use it reasonably. Constructing practical integrated QKD networks based on untrusted nodes will become a reality soon.

ACKNOWLEDGMENTS

This work was supported by the Fundamental Research Funds for the Central Universities, the National Natural Science Foundation of China (Grant No. 62105318, 62271463, 62171424, 62301524), the China Postdoctoral Science Foundation (Grant No. 2021M693098, 2022M723064), and the Innovation Program for Quantum Science and Technology (Grant No. 2021ZD0300700).

APPENDIX A: SPECIFIC FORMS OF GAIN AND SUPPRESSION TERMS IN THE GAIN-SUPPRESSION FUNCTION

In this appendix, we give the specific form of the gain-suppression function. For simplicity, we derive the formulas on the basis of Eq. (1). Firstly, we give the special forms of the gain and error-rate terms contained in Eq. (1) as

$$\begin{aligned}
Y_{11} &= (1-Y_0/2)^2[\frac{\eta_A\eta_B}{2} + (2\eta_A + 2\eta_B - 3\eta_A\eta_B)Y_0/2 \\
&\quad + 4(1-\eta_A)(1-\eta_B)(Y_0/2)^2], \\
e_{11} &= e_0 - (e_0 - e_d)[1-(Y_0/2)^2]\frac{\eta_A\eta_B}{2Y_{11}}, \\
Q_{11} &= \mu_A\mu_B e^{-\mu_A-\mu_B}Y_{11}, \\
Q^C_{\rm rect} &= 2[1-(Y_0/2)]^2\exp(-\frac{\eta_A\mu_A+\eta_B\mu_B}{2}) \\
&\quad \times [1-(1-Y_0/2)e^{-\eta_A\mu_A/2}] \\
&\quad [1-(1-Y_0/2)e^{-\eta_B\mu_B/2}], \\
Q^E_{\rm rect} &= Y_0(1-Y_0/2)^2\exp(-\frac{\eta_A\mu_A+\eta_B\mu_B}{2}) \\
&\quad \times [I_0(\sqrt{\eta_A\mu_A\eta_B\mu_B}) - (1-Y_0/2) \\
&\quad \times \exp(-\frac{\eta_A\mu_A+\eta_B\mu_B}{2})], \\
Q_{\rm rect} &= Q^C_{\rm rect} + Q^E_{\rm rect}, \\
E_{\rm rect} &= [e_dQ^C_{\rm rect} + (1-e_d)Q^E_{\rm rect} + (1-e_d)]/Q_{\rm rect}, \qquad \text{(A1)}
\end{aligned}$$

where Y_{11} (Y_0) is the response possibility of single-photon states (background noise), η_A (η_B) is the transmission efficiency of the Alice-Charlie (Bob-Charlie) channel, $e_0 = 1/2$ is the error rate of background noise, e_d is the misalignment error rate of the MDI system, μ_A (μ_B) is the average photon number of the weak coherent pulse launched from Alice (Bob), and $I_0(x)$ is the modified Bessel function of the first kind. μ_A and μ_B will be optimized to achieve a higher key rate.

Considering the specific form of the binary Shannon function, we can rewrite the key-rate formula as

$$\begin{aligned}
\mathcal{R} = \frac{1}{2}\{&Q_{11} + Q_{11}e_{11}\log_2(e_{11}) \\
&+ Q_{11}(1-e_{11})\log_2(1-e_{11}) + f_eQ_{\rm rect}E_{\rm rect}\log_2(E_{\rm rect}) \\
&+ f_eQ_{\rm rect}(1-E_{\rm rect})\log_2(1-E_{\rm rect})\}. \qquad \text{(A2)}
\end{aligned}$$

For simplicity, we use different letters to replace each term in Eq. (A2), where

$$\begin{aligned}
\mathcal{A} &= Q_{11}, \\
\mathcal{B} &= Q_{11}e_{11}\log_2(e_{11}), \\
\mathcal{C} &= Q_{11}(1-e_{11})\log_2(1-e_{11}), \qquad \text{(A3)} \\
\mathcal{D} &= f_eQ_{\rm rect}E_{\rm rect}\log_2(E_{\rm rect}), \\
\mathcal{E} &= f_eQ_{\rm rect}(1-E_{\rm rect})\log_2(1-E_{\rm rect}).
\end{aligned}$$

The derivative functions are written as follows:

$$\begin{aligned}
\frac{\partial \mathcal{A}}{\partial \theta} &= \frac{\partial Q_{11}}{\partial \theta},\\
\frac{\partial \mathcal{B}}{\partial \theta} &= \frac{\partial Q_{11}}{\partial \theta}[e_{11}\log_2(e_{11})]\\
&\quad + \frac{\partial e_{11}}{\partial \theta}\left\{Q_{11}\left[\log_2(e_{11}) + \frac{1}{\ln 2}\right]\right\},\\
\frac{\partial \mathcal{C}}{\partial \theta} &= \frac{\partial Q_{11}}{\partial \theta}\left[(1-e_{11})\log_2(1-e_{11})\right]\\
&\quad - \frac{\partial e_{11}}{\partial \theta}\left\{Q_{11}\left[\log_2(1-e_{11}+\frac{1}{\ln 2})\right]\right\},\\
\frac{\partial \mathcal{D}}{\partial \theta} &= \frac{\partial Q_{\rm rect}}{\partial \theta}[f_e E_{\rm rect}\log_2(E_{\rm rect})]\\
&\quad + \frac{\partial E_{\rm rect}}{\partial \theta}\left\{f_e Q_{\rm rect}\left[\log_2(E_{\rm rect}) + \frac{1}{\ln 2}\right]\right\},\\
\frac{\partial \mathcal{E}}{\partial \theta} &= \frac{\partial Q_{\rm rect}}{\partial \theta}[f_e(1-E_{\rm rect})\log_2(1-E_{\rm rect})]\\
&\quad - \frac{\partial E_{\rm rect}}{\partial \theta}\left\{f_e Q_{\rm rect}\left[\log_2(1-E_{\rm rect}) + \frac{1}{\ln 2}\right]\right\}.
\end{aligned} \tag{A4}$$

Then we need to calculate the derivative functions of the response rate and the quantum bit error rate:

$$\begin{aligned}
\frac{\partial e_{11}}{\partial \theta} &= \frac{(e_d - e_0)\eta_A\eta_B}{2}\\
&\quad \times \left\{-Y_0\frac{\partial Y_0}{\partial \theta}Y_{11}^{-1} - \left[1-\left(\frac{Y_0}{2}\right)^2\right]Y_{11}^{-2}\frac{\partial Y_{11}}{\partial \theta}\right\},\\
\frac{\partial Q_{11}}{\partial \theta} &= \mu_A\mu_B e^{-\mu_A-\mu_B}\\
&\quad \times \left\{\frac{\partial Y_0}{\partial \theta}\left(1-\frac{Y_0}{2}\right)\left[\eta_A\eta_B\left(-2+\frac{17}{4}Y_0 - 2Y_0^2\right)\right.\right.\\
&\quad \left. + (\eta_A+\eta_B)\left(1-\frac{7}{2}Y_0+2Y_0^2\right) + 2Y_0(1-Y_0)\right]\\
&\quad + \frac{\partial \eta_A}{\partial \theta}\left[\left(1-\frac{Y_0}{2}\right)^2 Y_0(1-Y_0)\right]\\
&\quad \left. + \frac{\partial \eta_B}{\partial \theta}\left[\left(1-\frac{Y_0}{2}\right)^2 Y_0(1-Y_0)\right]\right\}\\
&= \mu_A\mu_B e^{-\mu_A-\mu_B}\frac{\partial Y_{11}}{\partial \theta},\\
\frac{\partial E_{\rm rect}}{\partial \theta} &= \frac{\partial Q_{\rm rect}^C}{\partial \theta}\\
&\quad \times \left[e_d Q_{\rm rect}^{-1} - e_d Q_{\rm rect}^C Q_{\rm rect}^{-2} - (1-e_d)Q_{\rm rect}^E Q_{\rm rect}^{-2}\right]\\
&\quad + \frac{\partial Q_{\rm rect}^E}{\partial \theta}\\
&\quad \times \left[-e_d Q_{\rm rect}^C Q_{\rm rect}^{-2} + (1-e_d)(Q_{\rm rect}^{-1} - Q_{\rm rect}^E Q_{\rm rect}^{-2})\right],\\
\frac{\partial Q_{\rm rect}}{\partial \theta} &= \frac{\partial Q_{\rm rect}^C}{\partial \theta} + \frac{\partial Q_{\rm rect}^E}{\partial \theta},\\
\frac{\partial Q_{\rm rect}^C}{\partial \theta} &= 2\left(1-\frac{Y_0}{2}\right)\exp\left[-\frac{\eta_A\mu_A+\eta_B\mu_B}{2}\right]\\
&\quad \times \left\{\frac{\partial Y_0}{\partial \theta}\left[-\mathcal{X}\mathcal{Y} + \frac{1}{2}(1-\frac{Y_0}{2})\left(e^{-\frac{\eta_A\mu_A}{2}}\mathcal{Y}\right.\right.\right.\\
&\quad \left.\left.\left. + e^{-\frac{\eta_B\mu_B}{2}}\mathcal{X}\right)\right] + \frac{\partial \eta_A}{\partial \theta}\left[-\left(1-\frac{Y_0}{2}\right)\frac{\mu_A}{2}\mathcal{X}\mathcal{Y}\right.\right.\\
&\quad \left.\left. - \left(1-\frac{Y_0}{2}\right)^2\frac{\mu_A}{2}e^{-\frac{\eta_A\mu_A}{2}}\mathcal{Y}\right]\right.\\
&\quad + \frac{\partial \eta_B}{\partial \theta}\left[-\left(1-\frac{Y_0}{2}\right)\frac{\mu_B}{2}\mathcal{Y}\mathcal{X}\right.\\
&\quad \left.\left. - \left(1-\frac{Y_0}{2}\right)^2\frac{\mu_B}{2}e^{-\frac{\eta_B\mu_B}{2}}\mathcal{X}\right]\right\},\\
\frac{\partial Q_{\rm rect}^E}{\partial \theta} &= \left(1-\frac{Y_0}{2}\right)\exp\left[-\frac{\eta_A\mu_A+\eta_B\mu_B}{2}\right]\\
&\quad \times \left\{\frac{\partial Y_0}{\partial \theta}\left[\left(1-\frac{3Y_0}{2}\right)\mathcal{Z}\right.\right.\\
&\quad \left. + \frac{1}{2}Y_0\left(1-\frac{Y_0}{2}\right)e^{-\frac{\eta_A\mu_A+\eta_B\mu_B}{2}}\right]\\
&\quad - \frac{\partial \eta_A}{\partial \theta}Y_0\left(1-\frac{Y_0}{2}\right)\frac{\mu_A}{2}\\
&\quad \times \left[\mathcal{Z} - \left(1-\frac{Y_0}{2}e^{-\frac{\eta_A\mu_A+\eta_B\mu_B}{2}}\right)\right]\\
&\quad - \frac{\partial \eta_B}{\partial \theta}Y_0\left(1-\frac{Y_0}{2}\right)\frac{\mu_B}{2}\\
&\quad \left.\left. \times \left[\mathcal{Z} - \left(1-\frac{Y_0}{2}e^{-\frac{\eta_A\mu_A+\eta_B\mu_B}{2}}\right)\right]\right\},
\end{aligned} \tag{A5}$$

where the auxiliary variables $\mathcal{X}$, $\mathcal{Y}$, and $\mathcal{Z}$ are given by

$$\begin{aligned}
\mathcal{X} &= 1-\left(1-\frac{Y_0}{2}\right)\exp\left[-\frac{\eta_A\mu_A}{2}\right],\\
\mathcal{Y} &= 1-\left(1-\frac{Y_0}{2}\right)\exp\left[-\frac{\eta_B\mu_B}{2}\right],\\
\mathcal{Z} &= 1+\frac{\eta_A\mu_A\eta_B\mu_B}{4} - \left(1-\frac{Y_0}{2}\right)\exp\left[-\frac{\eta_A\mu_A+\eta_B\mu_B}{2}\right].
\end{aligned} \tag{A6}$$

The derivative functions of η_A (η_B) and Y_0, $\partial\eta_A/\partial\theta$ ($\partial\eta_B/\partial\theta$) and $\partial Y_0/\partial\theta$, are easy to derive, and are written as

$$\frac{\partial Y_0}{\partial\theta} = P_{\text{system}} \times \left\{10^{\left[-1-\frac{\alpha L\theta}{10(1+\theta)}\right]}\frac{10+\theta(10-\alpha L\ln 10)}{(1+\theta)^3}\right\} - \frac{P_{\text{system}}}{2(1+\theta)^2} \times \left\{10^{\left[-\frac{\alpha L\theta}{10(1+\theta)}\right]} + 10^{\left[-\frac{\alpha L(2+\theta)}{10(1+\theta)}\right]}\right\},$$

$$\frac{\partial\eta_A}{\partial\theta} = \frac{\eta_d 10^{\left[-\frac{\alpha L\theta}{10(1+\theta)}\right]}}{10(1+\theta)^2}, \quad \frac{\partial\eta_A}{\partial\theta} = -\frac{\eta_B}{\eta_A}\frac{\partial\eta_A}{\partial\theta},$$

$$P_{\text{system}} = \frac{\rho T_d\lambda_q\eta_d\Delta\lambda P_A L}{2hc}. \tag{A7}$$

After rearranging the equations above, we can derive Eq. (6), and thus we reveal the gain-suppression relationship.

APPENDIX B: SPRS-NOISE MODEL AND EXPERIMENTAL VERIFICATION

The SPRS-noise model is the core of our asymmetric noise model; thus, its accuracy and the rationality of its parameters determine the validly of our conclusion. Here we provide a simple demonstration by studying the Raman coefficient, an intrinsic property of SMF.

SPRS noise can be divided into forward and backward noise by the direction. The noise-photon-number functions N_{forward} and N_{backward} can be written as [32]

$$N_{\text{forward}}(L,P) = \frac{\rho T_d\lambda_q\eta_d\Delta\lambda PL10^{-\alpha L/10}}{hc},$$
$$N_{\text{backward}}(L,P) = \frac{5\rho T_d\lambda_q\eta_d\Delta\lambda P(1-10^{-\alpha L/5})}{hc\alpha\ln 10}, \tag{B1}$$

where ρ is the Raman coefficient, T_d is the window time of the SPD, λ_q is the wavelength of the quantum channel, $\Delta\lambda$ is the bandwidth of the narrowband filter, h is the Planck constant, and c is the speed of light in a vacuum. In this work, we analyze the integration in the C band, and quantum and classical channels are both set at around 1550 nm, so we regard all the channels as having the same attenuation efficiency α. A typical value of around 20 km can be extracted from the equations above, where the generation and attenuation of noise photons are equal, producing noise peaks or a noise platform as shown in many previous studies [19].

The accuracy of the SPRS-noise model has been tested hundreds of times in previous studies [18–20], but the problem remains of whether the value of ρ is effective. We designed a simple experiment for the test (Fig. 8).

A tunable laser emits continuous light according to the channel frequency set by dense wavelength division multiplexing (DWDM) to simulate classical optical communication; the wavelength of light is chosen so as to avoid it coinciding with 1550.12 nm, which is reserved for the quantum channel. A 90:10 beam splitter separates some of the light intensity for power monitoring. Before the light enters DWDM, we use a variable optical attenuator to control the power of the incident light. After 50 km of SMF and DWDM, we connect superconductor nanowire single photon detector (SNSPD) at the output of the quantum channel to detect the Raman noise generated by the classical channel. By adjusting the variable optical attenuator, we obtain a series of noise counts at different incident powers to calculate the Raman coefficient. The experimental parameters are listed in Table II.

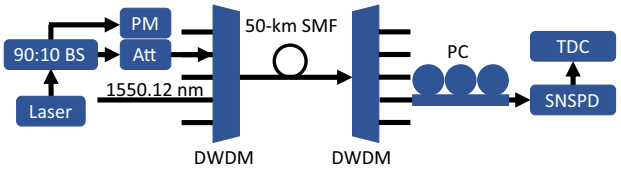

FIG. 8. Experimental setup for studying the Raman coefficient. A tunable laser simulates classical optical channels. Att, variable optical attenuator; BS, 90:10 beam splitter for power monitoring; PC, polarization controller; PM, power meter; TDC, time-to-digital converter.

By scanning different powers, we obtain the corresponding noise count and extract the specific value of the Raman coefficient from the slope using a linear-fitting method in Fig. 9. The Raman coefficient ρ we measured is $1.68\times10^{-9}\,\text{km}^{-1}\,\text{nm}^{-1}$, which is close to the value in previous work [32], and we chose the value as $1.59\times10^{-9}\,\text{km}^{-1}\text{nm}^{-1}$ in our simulation.

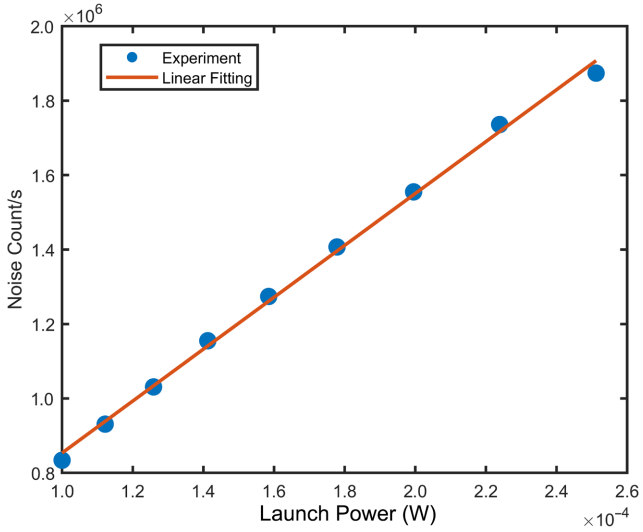

FIG. 9. Measured SPRS-noise count and linear-fitting line.

TABLE II. Parameters used for the experimental test.

Parameter	Value
Classical channel frequency	1547.72 nm
Quantum channel frequency λ_q	1550.12 nm
Fiber attenuation coefficient α	0.19 dB/km
Total insertion loss of DWDM	(2.48 + 3.63) dBm = 6.11 dB
Bandwidth of DWDM $\Delta\lambda$	0.48 nm
Channel spacing of DWDM	100 GHz
Detection efficiency of SNSPD η_d	80.48%
Accumulation time of SNSPD T_d	1 s
Dark count rate of SNSPD	2.4×10^{-8} per window

APPENDIX C: CONCLUSIONS WITH FINITE-SIZE EFFECTS

The finite-size effect affects the performance of QKD significantly, while our discussion concerns $N = 10^{11}$. The relationship between our conclusion and the finite-size effect deserves to be explored for deeper understanding. The fiber length and power are set as 40 km and −10.5 dBm, respectively, in the calculation with different N. The behaviors of the maximum-increase ratio are displayed in Fig. 10.

It seems that the finite-size effect affects our conclusion significantly, with small N bringing about greater improvement. The discussions above are limited by a specific integration environment, an absolute environment, whereas our conclusion depends on a relative environment, where the system is sensitive to noise. A key-rate-versus-launch-power diagram is shown in Fig. 11 to show the relative position of a particular environment in different systems. Obviously, −10.5-dBm launch power (9×10^{-5} W) is located in different regions of the curves. The noise causes only a weak decrease for the orange curve, but the blue curve suffers a key-rate drop of 1–2 orders of magnitude. Connected with the results in Fig. 10, the enhancement of our conclusions depends only on whether the system is sensitive to noise in a given integration environment, and we can predict that if the launch power is high enough (2.1×10^{-4} W), a significant improvement should also be observed in systems with a pulse number of 1×10^{20}. The finite-size effect can affect the absolute key-rate level. However, for our conclusions, this effect is the same as with other factors such as distance and power that influence the noise sensitivity of QKD systems. Smaller N makes the system more sensitive, where the asymmetry works efficiently in key-rate increase.

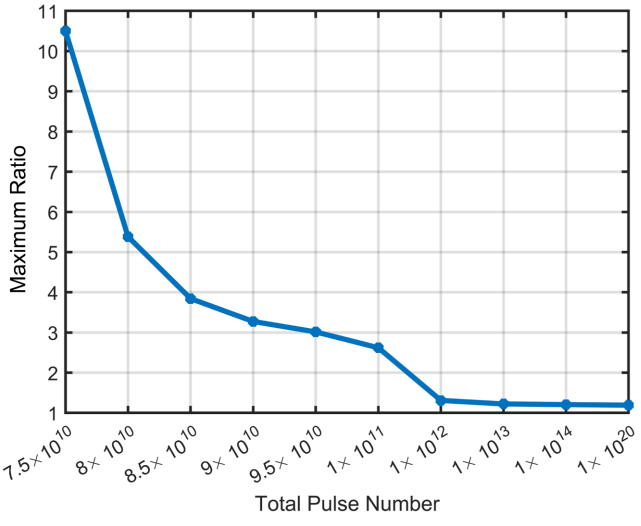

FIG. 10. Evolution of the maximum ratio with different total pulse numbers in a typical integration environment.

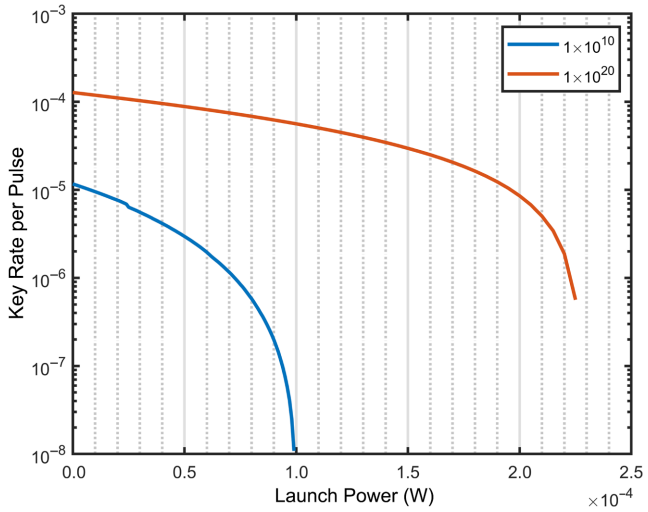

FIG. 11. Relative position of a particular environment in different systems. Orange and blue curves represent the key-rate–power relationship in systems with $N = 1 \times 10^{20}$ and $N = 1 \times 10^{11}$. The total fiber length is set as 40 km.

[1] N. Gisin, G. Ribordy, W. Tittel, and H. Zbinden, Quantum cryptography, Rev. Mod. Phys. **74**, 145 (2002).

[2] B. Qi, L. Qian, and H.-K. Lo, A brief introduction of quantum cryptography for engineers, arXiv:1002.1237 [quant-ph] (2010).

[3] T. E. Chapuran, P. Toliver, N. A. Peters, J. Jackel, M. S. Goodman, R. J. Runser, S. R. McNown, N. Dallmann, R. J. Hughes, K. P. McCabe, J. E. Nordholt, C. G. Peterson, K. T. Tyagi, L. Mercer, and H. Dardy, Optical networking for quantum key distribution and quantum communications, New J. Phys. **11**, 105001 (2009).

[4] G.-J. Fan-Yuan, F.-Y. Lu, S. Wang, Z.-Q. Yin, D.-Y. He, Z. Zhou, J. Teng, W. Chen, G.-C. Guo, and Z.-F. Han, Measurement-device-independent quantum key distribution for nonstandalone networks, Photon. Res. **9**, 1881 (2021).

[5] C. Cai, Y. Sun, J. Niu, P. Zhang, Y. Zhang, and Y. Ji, Multicore-fiber-based quantum-classical access network architecture with quantum signal wavelength-time division multiplexing, J. Opt. Soc. Am. B **37**, 1047 (2020).

[6] G.-J. Fan-Yuan, F.-Y. Lu, S. Wang, Z.-Q. Yin, D.-Y. He, W. Chen, Z. Zhou, Z.-H. Wang, J. Teng, G.-C. Guo, and Z.-F. Han, Robust and adaptable quantum key distribution network without trusted nodes, Optica **9**, 812 (2022).

[7] V. Scarani, H. Bechmann-Pasquinucci, N. J. Cerf, M. Dušek, N. Lütkenhaus, and M. Peev, The security of practical quantum key distribution, Rev. Mod. Phys. **81**, 1301 (2009).

[8] F. Xu, X. Ma, Q. Zhang, H.-K. Lo, and J.-W. Pan, Secure quantum key distribution with realistic devices, Rev. Mod. Phys. **92**, 025002 (2020).

[9] C. Portmann and R. Renner, Security in quantum cryptography, Rev. Mod. Phys. **94**, 025008 (2022).

[10] W. Chen, Z.-F. Han, T. Zhang, H. Wen, Z.-Q. Yin, F.-X. Xu, Q.-L. Wu, Y. Liu, Y. Zhang, X.-F. Mo, and Y. Z. Gui, Field experiment on a "star type" metropolitan quantum key distribution network, IEEE Photonics Technol. Lett. **21**, 575 (2009).

[11] S. Wang, W. Chen, Z.-Q. Yin, Y. Zhang, T. Zhang, H.-W. Li, F.-X. Xu, Z. Zhou, Y. Yang, D.-J. Huang, L.-J. Zhang, F.-Y. Li, D. Liu, Y.-G. Wang, G.-C. Guo, and Z.-F. Han, Field test of wavelength-saving quantum key distribution network, Opt. Lett. **35**, 2454 (2010).

[12] T.-Y. Chen, J. Wang, H. Liang, W.-Y. Liu, Y. Liu, X. Jiang, Y. Wang, X. Wan, W.-Q. Cai, L. Ju, L.-K. Chen, L.-J. Wang, Y. Gao, K. Chen, C.-Z. Peng, Z.-B. Chen, and J.-W. Pan, Metropolitan all-pass and inter-city quantum communication network, Opt. Express **18**, 27217 (2010).

[13] S. Wang *et al.*, Field and long-term demonstration of a wide area quantum key distribution network, Opt. Express **22**, 21739 (2014).

[14] J.-Y. Liu, X. Ma, H.-J. Ding, C.-H. Zhang, X.-Y. Zhou, and Q. Wang, Experimental demonstration of five-intensity measurement-device-independent quantum key distribution over 442 km, Phys. Rev. A **108**, 022605 (2023).

[15] I. Choi, R. J. Young, and P. D. Townsend, Quantum key distribution on a 10Gb/s WDM-PON, Opt. Express **18**, 9600 (2010).

[16] P. D. Townsend, Simultaneous quantum cryptographic key distribution and conventional data transmission over installed fibre using wavelength-division multiplexing, Electron. Lett. **33**, 188 (1997).

[17] C. H. Bennett and G. Brassard, in *Proceedings of IEEE International Conference on Computers, Systems, and Signal Processing* (IEEE, New York, 1984), p. 175.

[18] J.-Q. Geng, G.-J. Fan-Yuan, S. Wang, Q.-F. Zhang, W. Chen, Z.-Q. Yin, D.-Y. He, G.-C. Guo, and Z.-F. Han, Quantum key distribution integrating with ultra-high-power classical optical communications based on ultra-low-loss fiber, Opt. Lett. **46**, 6099 (2021).

[19] K. A. Patel, J. F. Dynes, I. Choi, A. W. Sharpe, A. R. Dixon, Z. L. Yuan, R. V. Penty, and A. J. Shields, Coexistence of high-bit-rate quantum key distribution and data on optical fiber, Phys. Rev. X **2**, 041010 (2012).

[20] J.-Q. Geng, G.-J. Fan-Yuan, S. Wang, Q.-F. Zhang, Y.-Y. Hu, W. Chen, Z.-Q. Yin, D.-Y. He, G.-C. Guo, and Z.-F. Han, Coexistence of quantum key distribution and optical transport network based on standard single-mode fiber at high launch power, Opt. Lett. **46**, 2573 (2021).

[21] F. Grünenfelder, R. Sax, A. Boaron, and H. Zbinden, The limits of multiplexing quantum and classical channels: Case study of a 2.5 GHz discrete variable quantum key distribution system, Appl. Phys. Lett. **119**, 124001 (2021).

[22] C.-H. F. Fung, B. Qi, K. Tamaki, and H.-K. Lo, Phase-remapping attack in practical quantum-key-distribution systems, Phys. Rev. A **75**, 032314 (2007).

[23] F. Xu, B. Qi, and H.-K. Lo, Experimental demonstration of phase-remapping attack in a practical quantum key distribution system, New J. Phys. **12**, 113026 (2010).

[24] V. Makarov* and D. R. Hjelme, Faked states attack on quantum cryptosystems, J. Mod. Opt. **52**, 691 (2005).

[25] V. Makarov, A. Anisimov, and J. Skaar, Effects of detector efficiency mismatch on security of quantum cryptosystems, Phys. Rev. A **74**, 022313 (2006).

[26] V. Makarov and J. Skaar, Faked states attack using detector efficiency mismatch on SARG04, phase-time, DPSK, and Ekert protocols, arXiv preprint arXiv:quant-ph/0702262 (2007).

[27] H.-K. Lo, M. Curty, and B. Qi, Measurement-device-independent quantum key distribution, Phys. Rev. Lett. **108**, 130503 (2012).

[28] S. L. Braunstein and S. Pirandola, Side-channel-free quantum key distribution, Phys. Rev. Lett. **108**, 130502 (2012).

[29] R. Valivarthi, P. Umesh, C. John, K. A. Owen, V. B. Verma, S. W. Nam, D. Oblak, Q. Zhou, and W. Tittel, Measurement-device-independent quantum key distribution coexisting with classical communication, Quantum Sci. Technol. **4**, 045002 (2019).

[30] R. C. Berrevoets, T. Middelburg, R. F. Vermeulen, L. D. Chiesa, F. Broggi, S. Piciaccia, R. Pluis, P. Umesh, J. F. Marques, W. Tittel, and Joshua A. Slater, Deployed measurement-device independent quantum key distribution and Bell-state measurements coexisting with standard internet data and networking equipment, Commun. Phys. **5**, 1 (2022).

[31] C. Cai, Y. Sun, and Y. Ji, Simultaneous long-distance transmission of discrete-variable quantum key distribution and classical optical communication, IEEE Trans. Commun. **69**, 3222 (2021).

[32] P. Eraerds, N. Walenta, M. Legré, N. Gisin, and H. Zbinden, Quantum key distribution and 1 Gbps data encryption over a single fibre, New J. Phys. **12**, 063027 (2010).

[33] W. Wang, F. Xu, and H.-K. Lo, Asymmetric protocols for scalable high-rate measurement-device-independent quantum key distribution networks, Phys. Rev. X **9**, 041012 (2019).

[34] D. Chen, Z. Shang-Hong, Z. Wei-Hu, S. Lei, and Z. Gu-Hao, Analysis of measurement-device-independent quantum key distribution under asymmetric channel transmittance efficiency, Quantum Inf. Process. **13**, 2525 (2014).

[35] H. Liu, W. Wang, K. Wei, X.-T. Fang, L. Li, N.-L. Liu, H. Liang, S.-J. Zhang, W. Zhang, H. Li, L. You, Z. Wang, H.-K. Lo, T.-Y. Chen, F. Xu, and J.-W. Pan, Experimental demonstration of high-rate measurement-device-independent quantum key distribution over asymmetric channels, Phys. Rev. Lett. **122**, 160501 (2019).

[36] Y.-L. Tang, H.-L. Yin, S.-J. Chen, Y. Liu, W.-J. Zhang, X. Jiang, L. Zhang, J. Wang, L.-X. You, J.-Y. Guan, D.-X. Yang, Z. Wang, H. Liang, Z. Zhang, N. Zhou, X. Ma, T.-Y. Chen, Q. Zhang, and J.-W. Pan, Measurement-device-independent quantum key distribution over 200 km, Phys. Rev. Lett. **113**, 190501 (2014).

[37] X. Ma and M. Razavi, Alternative schemes for measurement-device-independent quantum key distribution, Phys. Rev. A **86**, 062319 (2012).

[38] Q. Wang and X.-B. Wang, Simulating of the measurement-device independent quantum key distribution with phase randomized general sources, Sci. Rep. **4**, 4612 (2014).

[39] W.-Y. Hwang, Quantum key distribution with high loss: Toward global secure communication, Phys. Rev. Lett. **91**, 057901 (2003).

[40] H.-K. Lo, X. Ma, and K. Chen, Decoy state quantum key distribution, Phys. Rev. Lett. **94**, 230504 (2005).

[41] X.-B. Wang, Beating the photon-number-splitting attack in practical quantum cryptography, Phys. Rev. Lett. **94**, 230503 (2005).

[42] C. Jiang, Z.-W. Yu, X.-L. Hu, and X.-B. Wang, Higher key rate of measurement-device-independent quantum key distribution through joint data processing, Phys. Rev. A **103**, 012402 (2021).

[43] M. Lucamarini, Z. L. Yuan, J. F. Dynes, and A. J. Shields, Overcoming the rate–distance limit of quantum key distribution without quantum repeaters, Nature **557**, 400 (2018).

[44] X.-Y. Zhou, C.-H. Zhang, C.-M. Zhang, and Q. Wang, Asymmetric sending or not sending twin-field quantum key distribution in practice, Phys. Rev. A **99**, 062316 (2019).